JOURNAL OF COMPUTATIONAL PHYSICS 63, 434–457 (1986)

An Implicit Moment Electromagnetic Plasma Simulation in Cylindrical Coordinates

JON M. WALLACE, JEREMIAH U. BRACKBILL, AND DAVID W. FORSLUND

Applied Theoretical Physics Division, Los Alamos National Laboratory, Los Alamos, New Mexico 87545

Received November 5, 1984; revised March 6, 1985

An electromagnetic PIC plasma simulation code incorporating the implicit moment method and a two-dimensional cylindrical mesh, with r- and z-coordinate dependence, has been developed. The code is an extension of the VENUS code from the original two-dimensional Cartesian mesh. The physical model employed in the code will be discussed, with emphasis on aspects unique to cylindrical geometry. An application to self-generated magnetic fields and electron transport in a laser-irradiated disk is presented that highlights the usefulness of cylindrical coordinates. © 1986 Academic Press, Inc.

INTRODUCTION

An implicit moment method for nonrelativistic electromagnetic plasma simulation in two dimensions has recently been developed [1]. The method, introduced by Mason [2] in an electrostatic context, employs a new way of advancing in time the coupled particle and field equations that eliminates many of the numerical constraints on time and space steps encountered in explicit plasma simulation codes. With the implicit method, it is not necessary to resolve the electron plasma oscillations or the propagation of light waves. Computations which follow in detail only the ions and still remain numerically stable are possible. Likewise, it is unnecessary to resolve the Debye length. The method makes accessible to simulation larger time and space scales than are practical with an explicit formulation of the Maxwell–Vlasov equations. This is especially useful when simulating low-frequency plasma phenomena in which the high-frequency component of the electron motion is physically insignificant and only the average electron motion, where the high-frequency component has been removed, need to be considered.

The implicit moment method has been employed in the VENUS PIC code using the usual Cartesian grid [1]. However, because the implicit method makes possible the simulation of an entire plasma, including boundary effects, one is lead to incorporate the option of another mesh geometry. The two-dimensional Cartesian mesh is appropriate for a system which is infinite and perfectly homogeneous along the

0021-9991/86 $3.00

third Cartesian axis, frequently a reasonable approximation when modeling a small piece of a much larger physical system with an explicit simulation code. But a rectilinear mesh can be unrealistic for the simulation of an entire plasma and can lead to significant difficulty in the interpretation of the results. The most generally useful coordinates for representing bounded physical systems in two dimensions are cylindrical coordinates. One requires only that the physical system to be modeled possess symmetry, or approximate symmetry, with respect to some axis, often the case in practice. The radial and axial (r and z) dependences are incorporated in the particle and field equations, the single geometrical approximation being that all quantities in the system are indepedent of the azimuthal coordinate θ. All components of vector quantities are incorporated. Thus one obtains a true three-dimensional representation of any system which possesses azimuthal symmetry.

This paper describes the incorporation of cylindrical coordinates into the VENUS code. The general formulation of the implicit moment method for an electromagnetic plasma in cylindrical coordinates is given in Section 1. In Section 2, the advance of the particles in time is described in detail. Here it is shown how a Cartesian particle mover may be converted readily to a cylindrical particle mover. The solution algorithm for the field equations is discussed in Section 3. And in Section 4 an application, which demonstrates the utility of cylindrical coordinates, is presented. This is the problem of laser irradiation of the center of a disk-shaped foil. Comparisons of cylindrical and Cartesian simulations of the same system show significant differences in the self-generated magnetic fields and the magnetic-field induced surface electron transport, showing clearly the advantages of the more physical cylindrical mesh. Finally Section 5 is a brief summary of the work.

1. Formulation of the Implicit Moment Method for Electromagnetic Plasma Simulation

The implicit algorithm for the simulation of a plasma in an electromagnetic field is developed, starting from first principles.

a. *General Considerations*

The plasma simulation code describes a system of particles under the influence of Newton's law of motion,

$$\frac{d\mathbf{x}_{sp}}{dt} = \boldsymbol{u}_{sp}, \tag{1.1}$$

$$\frac{d\boldsymbol{u}_{sp}}{dt} = \frac{q_s}{m_s}\left(\mathbf{E} + \frac{\mathbf{u}_{sp}}{c} \times \mathbf{B}\right), \tag{1.2}$$

where s designates the particle type and p the particle index, q_s is the charge, and m_s is the mass of particle type s. The force on the r.h.s. of Eq. (1.2), purely elec-

tromagnetic in nature, is derived from self-consistent electric and magnetic fields **E** and **B**, satisfying Maxwell's equations. Introducing the usual scalar and vector potentials, Φ and **A**, we write

$$\mathbf{E} = -\nabla\Phi - \frac{1}{c}\frac{\partial \mathbf{A}}{\partial t}, \tag{1.3}$$

$$\mathbf{B} = \nabla \times \mathbf{A}. \tag{1.4}$$

The homogeneous Maxwell equations are then automatically satisfied and the inhomogeneous equations become

$$-\frac{1}{c^2}\frac{\partial^2 \mathbf{A}}{\partial t^2} + \nabla^2 \mathbf{A} = -\frac{4\pi}{c}\mathbf{J} + \frac{1}{c}\frac{\partial}{\partial t}(\nabla\Phi), \tag{1.5}$$

and

$$\nabla^2\Phi = -4\pi N, \tag{1.6}$$

where N is the net charge density and **J** is the net current density.

Additionally, computations are carried out in the Coulomb gauge so that

$$\nabla \cdot \mathbf{A} = 0. \tag{1.7}$$

In terms of the particle quantities, the densities are

$$N = \sum_s N_s = \sum_s q_s \int f_s(\mathbf{x}, \mathbf{u})\, d\mathbf{u}, \tag{1.8}$$

and

$$\mathbf{J} = \sum_s \mathbf{J}_s = \sum_s q_s \int \mathbf{u} f_s(\mathbf{x}, \mathbf{u})\, d\mathbf{u}, \tag{1.9}$$

where $f_s(\mathbf{x}, \mathbf{u})$ is the distribution function for particles of type s in **x**–**u** space. N and **J** are the zeroth and first moments of the distribution function. The system of equations to be solved is thus Eqs. (1.1), (1.2), (1.5), and (1.6), with the fields and potentials related by (1.3) and (1.4) and the density functions given by (1.8) and (1.9). We shall now develop the finite-difference form of these equations.

Conservative, central spatial differencing, described in the Appendix, is employed. The time differencing, which is not standard, is discussed in the next section.

b. *Time Differencing*

Considering first the time variable, the equations are finite differenced as follows [1]:

$$\mathbf{x}_{sp}^{n+1} - \mathbf{x}_{sp}^{n} = \mathbf{u}_{sp}^{n+1/2}\Delta t, \tag{1.10}$$

$$\mathbf{u}_{sp}^{n+1} - \mathbf{u}_{sp}^{n} = \frac{q_s}{m_s}\left(\mathbf{E}^{n+\theta} + \frac{\mathbf{u}_{sp}^{n+1/2}}{c} \times \mathbf{B}^{n}\right) \Delta t, \tag{1.11}$$

$$\nabla^2 \mathbf{A}^{n+\theta} - \frac{1}{\theta(c\Delta t)^2}\mathbf{A}^{n+\theta} = -\frac{4\pi}{c}\mathbf{J}^{n+1/2} + \frac{1}{\theta(c\Delta t)}(\nabla \Phi^{n+\theta} - \nabla \Phi^{n}) - \frac{1}{\theta(c\Delta t)^2}[(1+\theta)\mathbf{A}^{n} - \theta \mathbf{A}^{n-1}], \tag{1.12}$$

and

$$\nabla^2 \Phi^{n+\theta} = -4\pi N^{n+\theta}. \tag{1.13}$$

The superscript indicates the time in units of Δt, the time unit to be used for the remainder of this paper. θ is a parameter lying in the range $0 \leqslant \theta \leqslant 1$.

In the original VENUS code, the time step Δt is chosen so that

$$O(10^{-1}) < \frac{v_{th}\Delta t}{\Delta x} < O(1), \tag{1.14}$$

where v_{th} is the average thermal speed of the fastest particle type and Δx is the mesh interval. In the modified version of the code presented here, without an explicit pressure, the upper Courant limit is replaced by a turning point restriction on the particle orbits [3, 4]. The lower limit is imposed by the finite grid instability [1]. The parameter θ is chosen as in Ref. [1].

The fields are derived from the potentials according to

$$\mathbf{E}^{n+\theta} = -\nabla \Phi^{n+\theta} - \frac{\mathbf{A}^{n+\theta} - \mathbf{A}^{n}}{\theta c \Delta t}, \tag{1.15}$$

and

$$\mathbf{B}^{n} = \nabla \times \mathbf{A}^{n}. \tag{1.16}$$

After a solution for the above fields has been obtained, the vector potential is advanced in time according to

$$\mathbf{A}^{n+1} = \mathbf{A}^{n} + \frac{\mathbf{A}^{n+\theta} - \mathbf{A}^{n}}{\theta}. \tag{1.17}$$

The density functions are given by

$$N^{n+\theta}(\mathbf{x}) = \sum_s q_s \sum_p h(\mathbf{x} - \mathbf{x}_{sp}^{n+\theta})/(2\pi r\, \Delta r\, \Delta z), \tag{1.18}$$

and

$$\mathbf{J}^{n+1/2}(\mathbf{x}) = \sum_s q_s \sum_p \mathbf{u}_{sp}^{n+1/2} h(\mathbf{x} - \mathbf{x}_{sp}^{n+1/2})/(2\pi r\, \Delta r\, \Delta z), \tag{1.19}$$

where h is the particle-in-cell shape factor, to be discussed in Section 2.

It will be noted that the density functions required in Eqs. (1.12) and (1.13) are evaluated not at the beginning of the time interval, time n, but at some intermediate point in the interval. This is a manifestation of the implicitness of the scheme. However, before the field $\mathbf{E}^{n+\theta}$ has been found, the particle positions and velocities are known at no time later than n. Thus direct use of Eqs. (1.18) and (1.19), which require particle information at later times, would necessitate a simultaneous solution for particle *and* field quantities at intermediate times, a very time-consuming proposition. This difficulty is overcome by use of the *fluid* equations for N and $\mathbf{J}$ to extrapolate the known particle densities at time n, Eqs. (1.18) and (1.19) with θ and $\frac{1}{2}$ replaced by 0, a fraction of a time step ahead for substitution into the field equations. This is the essence of the implicit moment method. It makes possible a separation of the advance of the fields from that of the particles. No operations are performed on the particles during the field advance of a time step, which results in a considerable saving of machine time. We shall now show how this proceeds.

The equation for the charge density, which we consider first, is the continuity equation,

$$\frac{\partial N}{\partial t} + \mathbf{V} \cdot \mathbf{J} = 0. \tag{1.20}$$

The finite difference form of this equation, consistent with Eq. (1.10), is

$$N_s^{n+\theta} = N_s^n - \nabla \cdot \mathbf{J}_s^{n+1/2}(\theta \Delta t). \tag{1.21}$$

Thus the current density at time $n + 1/2$ is the remaining quantity required to close the system of equations. This may be obtained by using Eq. (1.11), with the replacement $\Delta t \to \Delta t/2$, to rewrite $\mathbf{u}_{sp}^{n+1/2}$ in Eq. (1.19). The result is

$$\mathbf{J}_s^{n+1/2}(\mathbf{x}) = q_s \sum_p \left[\mathbf{u}_{sp}^n + \frac{q_s}{m_s} \left(\mathbf{E}^{n+\theta} + \frac{\mathbf{u}_{sp}^{n+1/2}}{c} \times \mathbf{B}^n \right) \Delta t/2 \right] \times h(\mathbf{x} - \mathbf{x}_{sp}^{n+1/2})/(2\pi r \, \Delta r \, \Delta z). \tag{1.22}$$

Making the approximations that particle accelerations are sufficiently small that $(\Delta t)^2$-contributions may be dropped from the first term of Eq. (1.22) and summing the second term exactly, we obtain

$$\mathbf{J}_s^{n+1/2}(\mathbf{x}) = \tilde{\mathbf{J}}_s^{n+1/2}(\mathbf{x}) + \frac{q_s}{m_s} \left[N_s^{n+1/2} \, \mathbf{E}^{n+\theta} + \frac{\mathbf{J}_s^{n+1/2} \times \mathbf{B}^n}{c} \right] (\Delta t/2), \tag{1.23}$$

where

$$\tilde{\mathbf{J}}_s^{n+1/2}(\mathbf{x}) = q_s \sum_p \mathbf{u}_{sp}^n \, h(\mathbf{x} - \mathbf{x}_{sp}^n - \mathbf{u}_{sp}^n \, \Delta t/2)/(2\pi r \, \Delta r \, \Delta z). \tag{1.24}$$

$\tilde{\mathbf{J}}_s^{n+1/2}$ is the current density at time $n + 1/2$ that would have resulted from free

streaming of the particles after time n. (In the slightly more complicated formulation given in Ref. [4], the acceleration due to the magnetic field replaces the free-streaming motion.) Employing all the particle orbit information available at n, but no field information, $\tilde{J}_s^{n+1/2}$ is similar to a current-density estimate used in the direct method [3]. In this regard the present formulation is rather closer to the direct method with simplified differencing than was the formulation of Ref. [1]. It is within the $\tilde{J}$ term that the pressure tensor, which does not appear explicitly in this formulation, is embedded.[1] This formulation is adequate for weakly magnetized plasmas, i.e., for $\omega_{ce}\,\Delta t \ll 1$. Equation (1.23) may be rearranged so that $J_s^{n+1/2}$ is given explicitly.

$$\mathbf{J}_s^{n+1/2} = \hat{J}_s + \frac{q_s}{m_s}\frac{\hat{J}_s \times \mathbf{B}^n}{c}(\Delta t/2) + \left(\frac{q_s}{m_s}\right)^2 \frac{(\hat{J}_s \cdot \mathbf{B}^n)}{c^2}\mathbf{B}^n(\Delta t/2)^2, \tag{1.25}$$

where

$$\hat{J}_s \equiv \left[\tilde{J}_s^{n+1/2} + \frac{q_s}{m_s} N_s^{n+1/2}\mathbf{E}^{n+\theta}(\Delta t/2)\right]\frac{1}{1+(\omega_{cs}\Delta t/2)^2} \tag{1.26}$$

and

$$\omega_{cs} = \frac{q_s|\mathbf{B}^n|}{m_s c} \tag{1.27}$$

is the cyclotron frequency.

Analogously, Eq. (1.11) may be rearranged to give $\mathbf{u}_s^{n+1/2}$ explicitly, for use in Eq. (1.10).

$$\mathbf{u}_{sp}^{n+1/2} = \hat{u}_{sp} + \frac{q_s}{m_s}\frac{\hat{u}_{sp} \times \mathbf{B}^n}{c}(\Delta t/2) + \left(\frac{q_s}{m_s}\right)^2 \frac{(\hat{u}_{sp} \cdot \mathbf{B}^n)}{c^2}\mathbf{B}^n(\Delta t/2)^2, \tag{1.28}$$

where

$$\hat{u}_{sp} = \left[\mathbf{u}_{sp}^n + \frac{q_s}{m_s}\mathbf{E}^{n+\theta}(\Delta t/2)\right]\frac{1}{1+(\omega_{cs}\Delta t/2)^2}. \tag{1.29}$$

Intercomparison of Eqs. (1.25)–(1.29) shows in detail how the fluid description approximates the particle description. In the more precise particle description, Eqs. (1.28), (1.29), the fields are reevaluated for each particle at a point midway along the trajectory segment traversed between times n and $n+1$. In the fluid description, Eqs. (1.25), (1.26), the fields are evaluated at grid points and act on all particle fractions estimated to be located within the corresponding cell at time $n+1/2$. Different fractions of the same particle are subject to different fields centered in adjacent cells,

[1] The equivalent pressure tensor is $\tilde{P}_s = \sum_p (\mathbf{u}_{ps}^n - \bar{u}_s^n)(\mathbf{u}_{ps}^n - \bar{u}_s^n)\, h(\mathbf{x} - \mathbf{x}_{sp}^n - \mathbf{u}_{sp}^n\,\Delta t/2)/(2\pi r\,\Delta r\,\Delta z)$, where $\bar{u}_s^n = \sum_p \mathbf{u}_{ps}^n\, h(\mathbf{x} - \mathbf{x}_{sp}^n)/\sum_p h(\mathbf{x} - \mathbf{x}_{sp}^n)$.

but this is satisfactory for purposes of extrapolation over a fraction of a time step. The approximation propagates into the continuity equation (1.21), of course, the fluid analog of particle equation (1.10).

We now have a complete, self-consistent description of the physical system. The advance in time proceeds as follows: Assume the particle and field quantities $\mathbf{x}_{sp}^n$, $\mathbf{u}_{sp}^n$, $\mathbf{A}^n$, $\mathbf{A}^{n-1}$ are known for some n. Then N^n, $\mathbf{J}^n$ and $\tilde{J}^{n+1/2}$ are calculated from Eqs. (1.18) and (1.19), with θ and $\frac{1}{2}$ replaced by 0, and Eq. (1.24). Next Φ^n is calculated using Eq. (1.13) with $\theta = 0$. This ensures that the electrostatic potential at n is closely tied to the particle parameters and that the Coulomb-gauge relationship between Φ and N is preserved. Next $\mathbf{J}^{n+1/2}$, $N^{n+\theta}$, $\Phi^{n+\theta}$ and $\mathbf{A}^{n+\theta}$ are obtained by solving Eqs. (1.23), (1.21), (1.13), and (1.12) using an iterative procedure to be described in Section 3. Then $\mathbf{A}^{n+1}$ is evaluated using Eq. (1.17), $\mathbf{E}^{n+\theta}$ using Eq. (1.15), and $\mathbf{B}^{n+1}$ using Eq. (1.16). The particles are then advanced to time $n+1$ using Eqs. (1.28), (1.10), and (1.11). This completes the advance of one time step.

2. Advancing the Particles in Time

In this section we shall describe our method for advancing the particles in time in cylindrical coordinates. We begin with the specification of a PIC particle in the cylindrical mesh.

Each PIC particle is a three-dimensional entity, a cylindrical shell with constant radial thickness Δr and height Δz. See Fig. 1. The particles will thus fit precisely into a mesh cell, just as in the Cartesian case. The particle location in the mesh at time n is specified by the coordinates of the particle midpoint, r^n and z^n, in the radial and axial directions, where we have dropped the sp indices. Each PIC particle is imagined to contained the same large number of physical particles, electrons or ions. Following the usual Cartesian formulation, the density of real particles within a PIC particle at any given time is imagined to be constant, i.e., independent of location within the PIC particle volume. In particular, the physical particles are distributed uniformly in θ. Unlike the Cartesian case, however, the density of real particles in a PIC particle is not constant in time, but varies as $1/r^n$, reflecting the change in volume of the pseudoparticle as it moves in the radial direction. (An alternate formulation, which we have not pursued, is to imagine the physical particles as possessing a $1/r$ density variation within the PIC particle volume.) For the case of constant physical particle density, the number of computational particles per cell varies directly with r.

The motion of a particle at time n is specified by the three velocity coordinates u_r^n, u_θ^n, and u_z^n. Although the PIC particle has no azimuthal spatial coordinate, there is an azimuthal velocity component, which describes a rigid body rotation of all the contained real particles about the z-axis.

Following Boris [5], we employ a temporary Cartesian coordinate system for each particle as it is advanced. This system is oriented as shown in Fig. 2 so that its

x axis has some arbitrary direction perpendicular to the cylindrical z axis, while the z axis and origin of the temporary system coincide with those of the permanent cylindrical mesh. The arbitrariness arises from the fact that a PIC particle has no θ coordinate. With respect to this temporary Cartesian system, the particle positions and velocities at time n are

$$x^n = r^n,$$
$$z^n = z^n,$$
$$u_x^n = u_r^n,$$
$$u_y^n = u_\theta^n,$$

and

$$u_z^n = u_z^n, \tag{2.1}$$

where the cylindrical position and velocity components on the r.h.s. are those carried over from the previous time advance.

To advance the velocities, using Eqs. (1.28) and (1.29), we require the electric and magnetic fields at the particle location, along its trajectory, at time $n+1/2$. The particle location is first estimated from a free streaming approximation and then subsequently determined to greater accuracy by a Newton's method iteration, where each successive estimate of the particle parameters at $n+1/2$ is obtained using the fields and their first spatial derivatives at the previous estimate for the particle location at that time. The fields are determined at the particle location from particle-weighted averages of the cell-centered quantities

$$F_a(\mathbf{x}^{n+1/2}) = \sum_g h(\mathbf{x}^{n+1/2}, \mathbf{x}_g)\, F_a(\mathbf{x}_g), \tag{2.2}$$

where

$$a = r, \theta, \quad \text{or} \quad z, \qquad \text{the vector component,}$$
$$F = E^{n+\theta} \quad \text{or} \quad B^n,$$

and the summation is over all grid points. In the PIC formulation which we employ, there are at most 4 nonvanishing contributions to the summation. The weighting function, the particle-in-cell shape factor, is given by

$$h(\mathbf{x}^n, \mathbf{x}_g) = H(r_i - r^n, \Delta r)\, H(z_j - z^n, \Delta z) \left(\frac{1 + r_i/r^n}{2}\right), \tag{2.3}$$

where

$$H(x, \Delta x) = \begin{cases} 1 - |x|/\Delta x & \text{for} \quad |x| \leqslant \Delta x \\ 0 & \text{otherwise.} \end{cases}$$

The final factor, unique to cylindrical coordinates, reflects the radial dependence of both the PIC particle volume and the volume partitioning by the cell boundary surfaces. (In the alternate formulation where the real particles within a PIC particle are imagined to be distributed with a density $\rho \propto r^{-1}$ at any given time, this factor would disappear.) The weighting function has the usual normalization property,

$$\sum_g h(\mathbf{x}^n, \mathbf{x}_g) = 1. \tag{2.4}$$

The averaging procedure of Eq. (2.2) gives the magnitude for each field component in a coordinate system rotated slightly from our temporary Cartesian system, determined by $\mathbf{u}^{n+1/2}$ and r^n. In terms of the temporary Cartesian system

$$F_x = \cos(\gamma_{1/2})\, F_r(\mathbf{x}^{n+1/2}) - \sin(\gamma_{1/2})\, F_\theta(\mathbf{x}^{n+1/2}), \tag{2.5}$$

$$F_y = \sin(\gamma_{1/2})\, F_r(\mathbf{x}^{n+1/2}) + \cos(\gamma_{1/2})\, F_\theta(\mathbf{x}^{n+1/2}), \tag{2.6}$$

and

$$F_z = F_z(\mathbf{x}^{n+1/2}), \tag{2.7}$$

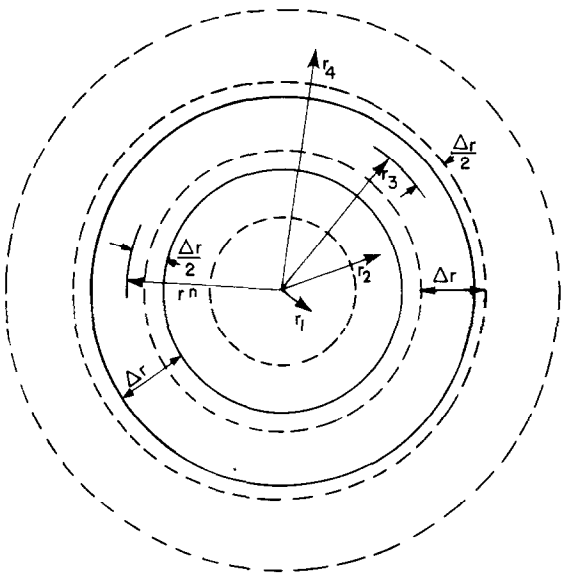

FIG. 1. View along the z axis of a PIC particle in the cylindrical mesh. The boundaries of the mesh cells are the dashed concentric circles with radial spacing Δr. The coordinates of the cells r_i specify the cell centers. Similarly the PIC particle, indicated by the solid circles, has a radial thickness Δr and a coordinate r^n which specifies its center at time n. The specification of the PIC particle with respect to the axial direction is the same as in the Cartesian case.

where the angle $\gamma_{1/2}$ is given by

$$\gamma_{1/2} = \tan^{-1}\left(\frac{u_y^{n+1/2}\,\Delta t/2}{r^n + u_x^{n+1/2}\,\Delta t/2}\right).$$

The velocities are now advanced to time $n+1/2$ in the temporary Cartesian system using Eqs.(1.28) and (1.29) with the fields given by Eqs. (2.5)–(2.7). Particle data from the previous iteration are used in the evaluation of the fields. All vector components in the equations of motion are specified with respect to the same set of unit vectors. Next the particle positions are advanced.

The advance in position along the z axis proceeds precisely as in the pure Cartesian case.

$$z^{n+1} = z^n + u_z^{n+1/2}\,\Delta t. \tag{2.8}$$

The advance in the radial direction, as can be seen from Fig. 2, is given by

$$r^{n+1} = (r^n + u_x^{n+1/2}\,\Delta t)\cos\gamma + (u_y^{n+1/2}\,\Delta t)\sin\gamma, \tag{2.9}$$

with

$$\gamma = \tan^{-1}\left(\frac{u_y^{n+1/2}\,\Delta t}{r^n + u_x^{n+1/2}\,\Delta t}\right). \tag{2.10}$$

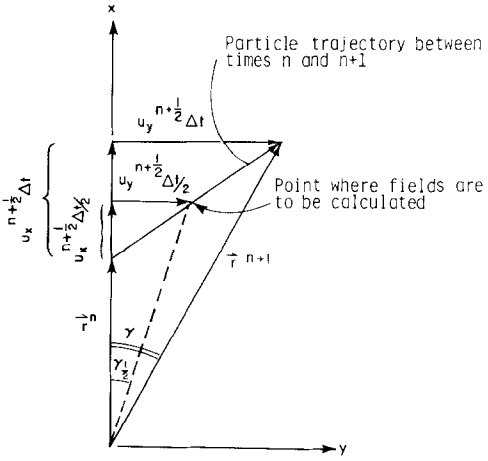

FIG. 2. Temporary local Cartesian coordinate system for advancing a particle from time $n\Delta t$ to $(n+1)\,\Delta t$. The z axis is directed into the page. The z axis and the origin coincide with those of the permanent cylindrical coordinate system. The motion of the particle is indicated, considering for simplicity only motion perpendicular to the z axis.

The velocity $\mathbf{u}^{n+1}$ is now obtained by first performing a linear extrapolation of $\mathbf{u}^n$ and $\mathbf{u}^{n+1/2}$ in the Cartesian system,

$$\mathbf{u}^{n+1} = 2\mathbf{u}^{n+1/2} - \mathbf{u}^n. \tag{2.11}$$

Then, the final step is to express $\mathbf{u}^{n+1}$ in the cylindrical system:

$$u_r^{n+1} = u_x^{n+1} \cos\gamma + u_y^{n+1} \sin\gamma,$$
$$u_\theta^{n+1} = -u_x^{n+1} \sin\gamma + u_y^{n+1} \cos\gamma,$$

and

$$u_z^{n+1} = u_z^{n+1}. \tag{2.12}$$

Note that the above formulae are correct even in the case $r^n + u_x^{n+1/2}\,\Delta t < 0$ with the convention $\tan^{-1}(a/b) = [\tan^{-1}(a/b)]_p + (1 - b/|b|)\,\pi/2$.

This procedure is repeated particle-by-particle. Aside from a sequence of coordinate rotations, the manipulations required are not different from those performed in the pure Cartesian case.

3. Advancing the Fields in Time

The field equations (1.12) and (1.13) are solved at time $n+\theta$ after the particles have been advanced to time n. The source functions $N^{n+\theta}$ and $\mathbf{J}^{n+1/2}$, obtained by extrapolation of the particle densities at n, using the moment equations (1.21) and (1.23), are themselves functions of $\mathbf{E}^{n+\theta}$. The source functions thus depend on both $\Phi^{n+\theta}$ and $\mathbf{A}^{n+\theta}$, and the field equations are not simply Poisson or Helmholz equations, as would be the case in a fully explicit scheme. As a result the field equations may not be solved by a single application of fast Fourier techniques. Here, instead, the field and fluid equations are solved simultaneously by an iterative method which makes repeated use of the Poisson–Helmholtz inversion. We proceed as follows.

First, the current densities are advanced to $n+1/2$, using $\mathbf{E}^n$ as a first estimate for $\mathbf{E}^{n+\theta}$ and $\mathbf{J}^n$ for $\mathbf{J}^{n+1/2}$ on the r.h.s. of Eq. (1.23). The result, a new estimate for $\mathbf{J}^{n+1/2}$, is then employed in Eq. (1.21) to advance the charge density to $n+\theta$. This estimate is next employed in Eq. (1.13) to give an estimate for $\Phi^{n+\theta}$. It has proved, however, to be necessary to introduce a pseudopotential at this point to make possible the convergence of the iteration procedure. The appropriate pseudopotential is found by shifting the dominant $\Phi^{n+\theta}$-term in $N^{n+\theta}$, which is second order in Δt, over to the l.h.s. of Eq. (1.13). We thus obtain

$$\nabla \cdot (1+\Omega)\,\nabla\Phi^{n+\theta} = -4\pi n^{n+\theta} + \nabla \cdot \Omega\nabla\Phi^{n+\theta}, \tag{3.1}$$

where

$$\Omega = 2\pi\theta(\Delta t)^2 \sum_s \frac{q_s}{m_s} N_s^n. \tag{3.2}$$

The only remaining $\Phi^{n+\theta}$-terms on the r.h.s. of Eq. (3.1) are third (and higher) order in Δt. On the basis of Eq. (3.1), we introduce the vector and scalar pseudopotentials,

$$\nabla\psi + \nabla \times \lambda = (1+\Omega)\,\nabla\Phi^{n+\theta}. \tag{3.3}$$

It is sufficient that λ possesses only a θ-component, so $\nabla \cdot \lambda = 0$ in the two-dimensional model. Substituting Eq. (3.3) into the l.h.s. of (3.1) gives

$$\nabla^2\psi^{l+1} = -4\pi N^{n+\theta} + \nabla \cdot \Omega(\nabla\Phi^{n+\theta})^l, \tag{3.4}$$

where l is the iteration index. The requirement $\nabla \times \nabla\Phi^{n+\theta} = 0$, which is not automatically satisfied after the pseudopotential is introduced, gives the equation for λ,

$$\nabla^2\lambda^{l+1} = [(\nabla\psi^{l+1} + \nabla \times \lambda^l) \times \nabla\beta]/(1-\beta), \tag{3.5}$$

where $\beta \equiv \Omega/(1+\Omega)$. The r.h.s. of Eq. (3.5) possesses only a θ-component. Thus, supposing ψ^l and λ^l are known, ψ^{l+1} is obtained by a Poisson inversion of Eq. (3.4). Then ψ^{l+1} and λ^l are substituted into the r.h.s. of Eq.(3.5), and which reduces to a Helmholtz equation for λ_θ. The one-component vector λ is thus obtained from a single Helmholtz inversion. The final step may be iterated by back substitution into the r.h.s. to give a more accurate solution for λ^{l+1}. A satisfactory starting point is $\lambda^0 \equiv 0$. The solutions ψ^{l+1} and λ^{l+1} are employed with Eq. (3.3) to reevaluate $-\nabla \cdot \Omega\nabla\Phi^{n+\theta}$, the dominant $\Phi^{n+\theta}$-term in $4\pi N^{n+\theta}$. A direct Poisson inversion of Eq. (1.13) is then performed to give a further improved estimate of $\nabla\Phi^{n+\theta}$. With this final step, $\nabla \times \nabla\Phi^{n+\theta} = 0$ precisely, and Faraday's law will be satisfied precisely, regardless of finite-difference or convergence considerations. The method of Concus and Golub [6] and [7] for inverting the modified two-dimensional Poisson operator, $\nabla \cdot a(x, y)\,\nabla$, can be used to accelerate convergence.

Next Eq. (1.12) is used to obtain an improved estimate of $\mathbf{A}^{n+\theta}$. Taking $\mathbf{A}^{n+\theta} \cong \mathbf{A}^n$ for the first approximation to the unknown vector potential, all quantities required on the r.h.s. are either known or have been estimated at this point. This time the dominant $\mathbf{A}^{n+\theta}$-term in $\mathbf{J}^{n+1/2}$ is shifted over to the l.h.s. of Eq. (1.12) after taking the maximum of the coefficient over the z direction. This gives a Helmholtz equation,

$$\nabla^2\mathbf{A}^{n+\theta} - \left[\frac{1}{\theta(c\,\Delta t)^2} + \alpha\right]\mathbf{A}^{n+\theta} = -\frac{4\pi}{c}\mathbf{J}^{n+1/2} - \alpha\mathbf{A}^{n+\theta} + \frac{\nabla\Phi^{n+\theta} - \nabla\Phi^n}{\theta c\,\Delta t}$$

$$- \frac{1}{\theta(c\,\Delta t)^2}[(1+\theta)\,\mathbf{A}^n - \theta\mathbf{A}^{n-1}], \tag{3.6}$$

where

$$\alpha(r) = \frac{2\pi}{c^2\theta} \max_z \left[\sum_s \frac{q_s}{m_s} N_s^n(r, z) \right]. \tag{3.7}$$

With the inversion of Eq. (3.6), we have from Eq. (1.15) a new estimate for $\mathbf{E}^{n+\theta}$. This quantity is used to initiate the next iteration, starting with the current-density advance. The procedure is repeated until a satisfactory degree of convergence is reached, typically in 20–50 iterations, with at most a small number $\leqslant 4$ of back substitutions of λ in Eq. (3.5) each iteration.

The electric field $\mathbf{E}^{n+\theta}$ obtained from this solution and the magnetic field $\mathbf{B}^n$ derived from the proceeding field solution are then employed to advance the particles from time n to $n+1$, as described in Section 2.

4. Application to Self-Generated Magnetic Fields and Superthermal Electron Transport in Laser-Irradiated Foils

One of the most interesting applications of plasma simulation methods is the computation of the response of a plasma to laser irradiation. The VENUS code with a Cartesian mesh has previously been employed for such simulations [8]. These computations have shown that electrons heated by the absorption of laser energy in a foil target generate strong magnetic fields of thermo-electric origin, which spread from the edge of the laser spot out along the target surface. The fields strongly influence the transport of superthermal electrons by the irradiation and can confine a large fraction of the deposition laser energy in the plasma blowoff region.

The Cartesian VENUS computations take the x axis to be perpendicular to the foil surface, with the y and z axes parallel to the surface. As all quantities in these simulations are z-independent, the computational system is effectively an infinitely long plasma strip, of finite width and thickness, with an infinitely long laser spot strip down the center. See Fig. 3. Such a setup is adequate for describing the general features of an irradiated plasma. However, it does not closely represent the common experimental geometry where a laser beam of circular cross section is focussed on the center of a disk-shaped foil target. In particular the spot to foil area ratio in the Cartesian setup can be an order of magnitude larger than in the experiment to be simulated. This introduces difficulties when detailed comparisons of simulation results and experiment are made, as will be shown in Section 4b. Clearly a cylindrical mesh is more appropriate for the simulation of these experiments. It provides a more qualitatively realistic picture of the magnetic field generation and the superthermal electron transport. In this section we present the results of a cylindrical VENUS simulation of a laser-irradiation experiment and compare them with the results of a Cartesian simulation.

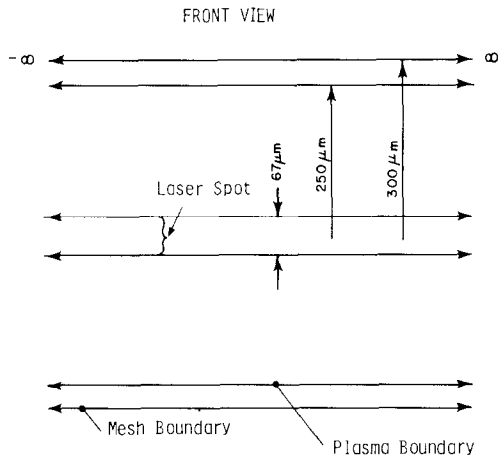

FIG. 3. Geometry for the Cartesian simulation of the laser-irradiated foil.

a. *Specification of the Simulations*

We consider the case of CO_2 laser irradiation of a 40 μm thick, 500 μm diameter disk. See Fig. 4. this is embedded in a computational mesh extending 50 μm beyond the side edge of the target and 160 μm in front of the target, the latter to accommodate plasma blowoff. One imagines the laser beam as entering from the front of the target and depositing energy into a spot region 135 μm in diameter and 10 μm thick centered about the critical surface of the plasma, i.e., the surface of critical density for CO_2 laser irradiation. The cylindrical mesh represents the geometry of this system exactly, while the Cartesian setup approximates the system by a 500 μm wide plasma strip and a 67 μm wide laser spot strip, as illustrated in Fig. 3. The smaller spot width will give **B**-fields of comparable spatial extent and magnitude to those in the cylindrical computation. The target is taken to be fully ionized hydrogen having the physical ion to electron mass ratio, 1836; initial thermal temperatures of $kT_e = 2.5$ keV and $kT_i = 0.1$ keV for the electrons and ions, respectively; and a density of $2\rho_c$, twice the critical density for the 10.6 μm laser wavelength. The density is ramped linearly to zero over a distance of 8 μm from the front and side plasma boundaries.

Intense CO_2 laser irradiation of a target produces highly energetic superthermal electrons near the critical surface, which take up most of the deposited energy. For purposes of the simulation, the laser energy deposition is approximated by a localized energy source in the plasma target. More specifically, kinetic energy is imparted to individual electrons inside the specified spot region so that they acquire a superthermal velocity distribution with a temperature $kT_h = 20$ keV. The rate at which energy is imparted to the plasma increases linearly with the time from zero to a maximum value of $\sim 5 \times 10^{13}$ W/cm^2 at $t = 11$ps. The irradiance is subsequently

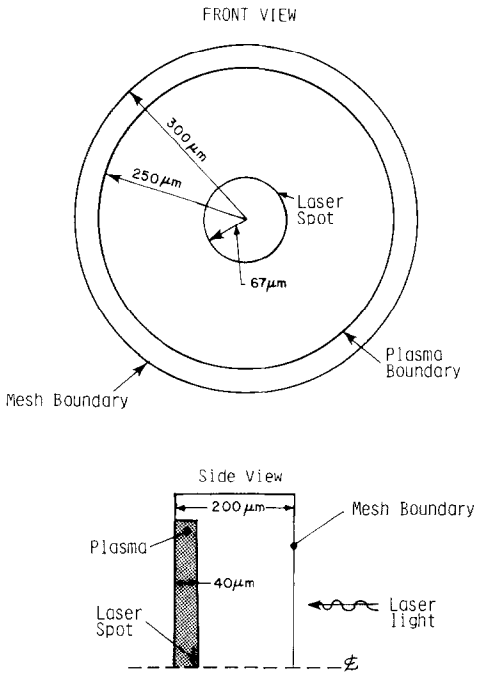

FIG. 4. Geometry for the cylindrical simulation of the laser-irradiated foil.

held constant. (This corresponds to a laser irradiance of $\sim 10^{14}$ W/cm^2, as typically one-third of the laser energy is absorbed by the target.)

The cylindrical simulation has 100 cells in the r direction and 128 in the z direction. The Cartesian simulation has 100 cells in the x direction and 256 in the y direction, which extends over a distance of twice the radius of the cylindrical geometry. There are 250,000 each of electron and ion pseudoparticles in the cylindrical computation and 500,000 in the Cartesian computation. The time step is $\Delta t = 2.5/\omega_{pe}$, with $\omega_{pe} = 1.78 \times 10^{14}\ \text{sec}^{-1}$, the frequency of CO_2 laser light. This value is sufficiently large that the finite grid instability does not develop, but is well below the electron Courant limit, c.f., Eq. (1.14).

b. *Results and Discussion*

We shall discuss the results of the simulations at a time of $t = 28.1$ ps, corresponding to the completion of 2000 computational cycles. At this time self-generated magnetic fields, produced by the plume of superthermal electrons which emerges from the laser spot and is directed back toward the incident beam, are well developed. Figure 5 shows a plot of the energy history for the cylindrical simulation. The largest energy component is the electron kinetic energy, accounting for $\sim 70\%$ of the energy in the system. It is relatively constant during the course of

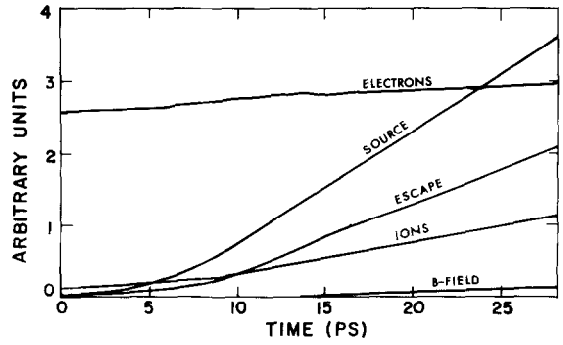

FIG. 5. Energy history for the cylindrical VENUS simulation. Each curve shows the energy versus time for the indicated plasma component.

the simulation. A comparable amount of energy is introduced into the system by the energy source. A large fraction, 57%, of the source energy, all of which is deposited into electrons, is subsequently transported by electrons across the rear and side boundaries of the mesh. Much of the remaining source energy, 28%, is imparted to ions by thermal and superthermal electrons. The rest of the source energy remains in electron energy, 10%, or goes into magnetic field energy, 2.7%. The energy partitioning for both the cylindrical and Cartesian simulations is summarized in Table I. The total energy in the system, taking into consideration source decomposition and boundary effects, is conserved to within 2%. Figure 6 shows the corresponding energy–history plot for the Cartesian simulation. The Cartesian and cylindrical results are quite comparable except for the background electron energy in the system. As would be expected, the Cartesian simulation has less background energy relative to the spot. Here, as in the cylindrical case, the electrons take up a large fraction of the energy in the system, and this energy component varies relatively slowly. And as before roughly half the source energy, 56%, is carried out of the system by electrons, which in this case is more than the electron energy in the

TABLE I

Normalized[a] Energy Components: Initial and Final

	Cylindrical geometry		Cartesian geometry	
	$t = 0$	$t = 28.1$ ps	$t = 0$	$t = 28.1$ ps
Electrons	0.956	1.090	0.956	1.319
Ions	0.044	0.410	0.044	0.756
Magnetic field	0.000	0.036	0.000	0.117
Electric field	0.000	0.005	0.000	0.036
Escaped	0.000	0.755	0.000	1.852
Source	0.000	1.322	0.000	3.293

[a] The energy components are normalized with respect to the total initial energy in the system.

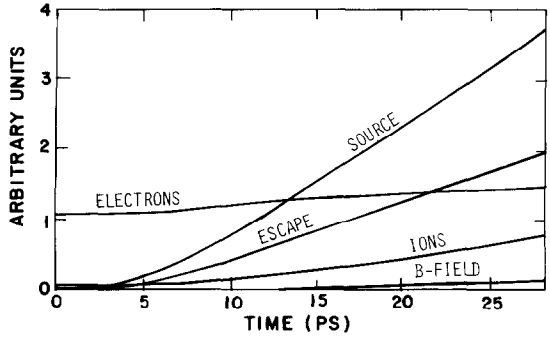

FIG. 6. Energy history for the Cartesian VENUS simulation. Each simulation. Each curve shows the energy versus time for the indicated plasma component.

mesh at late times. All the lost energy comes out the rear boundary in this calculation as periodic boundary conditions have been imposed in the y direction. A somewhat smaller fraction than in the cylindrical case, 22% of the source energy is imparted to ions, while 11% goes to electrons and 3.6% to the magnetic field. The ratio of ion to electron energy at late times is, however, larger. Energy is conserved in this calculation to within 6%. The nonconservation of energy appears to be associated with regions of the mesh most strongly affected by an imposed energy source. Energy is conserved better in the cylindrical computation because a smaller fraction of phase space is strongly influenced by the source. This can be seen from a comparison of Figs. 5 and 6, which shows how a larger relative amount of energy passes from the source into electrons and then out of the system in the Cartesian computation.

The cylindrical magnetic field results are shown in Fig. 7, a contour plot of B_θ, the dominant field component in this geometry. As there are relatively few computational particles in the small-radius region, the statistics are poor here and the small-radius fields are not expected to be particularly accurate. However, only the relatively few particles near $r = 0$ are affected by inaccurate fields. We thus ignore the high-gradient structure in the lower left corner of Fig. 7 and concentrate on the large-scale structure which covers much of the plot. The field reaches a maximum value of ~ 0.5 MG well out from the symmetry axis and just in front of the laser spot, where the electron plume is most well developed. The field falls off from this point in both the axial and radial directions. This can be seen more clearly from the field profile plots shown in Fig. 8. The radial fall-off outside the spot region has an approximate $1/r$-dependence. The field configuration in Cartesian geometry is different. Figure 9 shows the contour plot of B_z, the dominant field component in the Cartesian computation. The plot shows that the field dependence in the x direction is quite similar to the corresponding z-dependence in the cylindrical simulation, with maximum values of $\sim \pm 0.8$ MG occurring just in front of the laser deposition strip and near the strip edges. In contrast to the cylindrical results, the field does not fall off dramatically away from the laser strip in the y direction. The difference

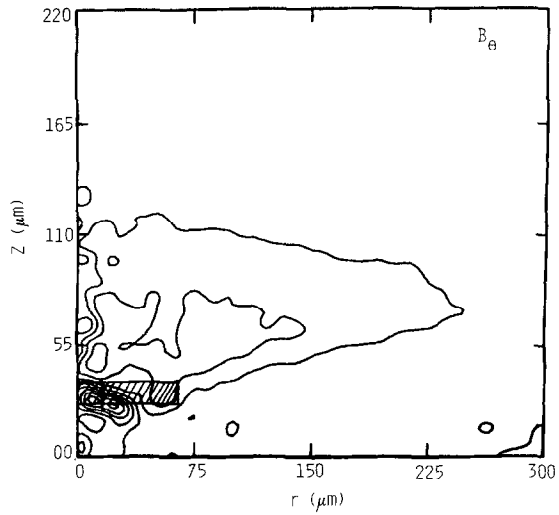

FIG. 7. Contour plot of B_θ obtained from the cylindrical VENUS computation at $t = 28.1$ ps. The energy deposition region at this time is indicated. The field component reaches a maximum value ~ 0.5 MG just in front of the laser spot.

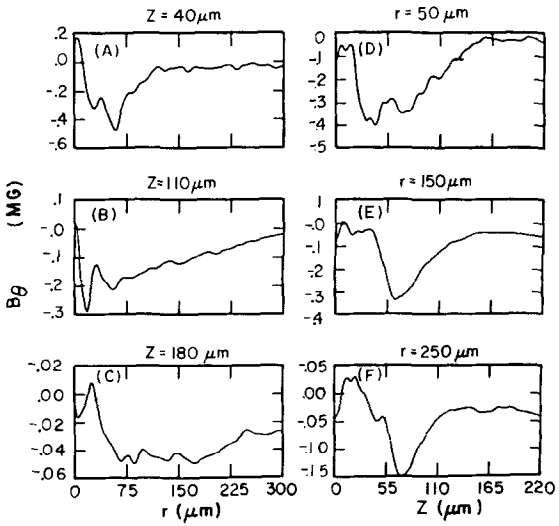

FIG. 8. Profile plots of B_θ obtained from the cylindrical VENUS simulation at $t = 28.1$ ps. Note the $1/r$ fall-off of the magnitude outside the laser spot most evident in (a).

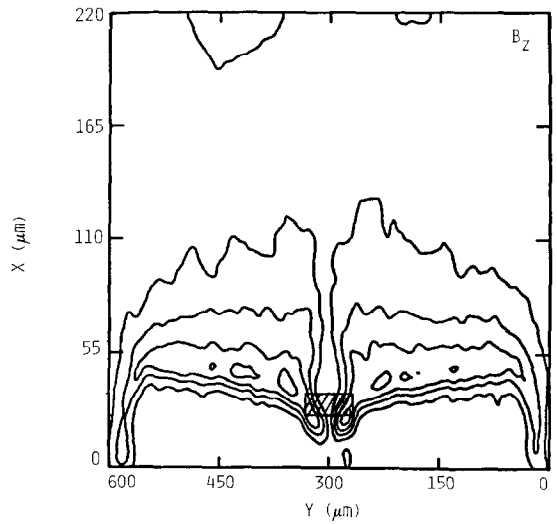

FIG. 9. Contour plot of B_z obtained from the Cartesian VENUS computation at $t = 16.9$ ps. The energy deposition region at this time is indicated. The field component has a maximum absolute value ~ 0.8 MG indicated by the two circular patterns just in front of the laser spot.

in the **B** field dependence along the front surface of the plasma can be qualitatively understood as follows: The plasma system is to a good approximation charge neutral so that $\nabla \cdot \mathbf{J} \simeq 0$. The lateral electron component is the dominant component of **J** in the low-density region in front of the plasma where **B** is large, i.e., $(J_e)_r$ in the cylindrical case and $(J_e)_y$ in the Cartesian case. Neglecting the other smaller components of **J**, charge neutrality gives rJ_r independent of r in the cylindrical case and J_y independent of y in the Cartesian case. Hence $B_\theta \propto 1/r$ in the one case and B_z is approximately independent of y in the other. The fall-off B_z near the y boundaries of the Cartesian simulation is the result of superthermal electrons propagating around the sides of the plasma, confining the field to the neighborhood of the target.

The lateral transport occurs when superthermal electrons, having been ejected from the laser deposition region, undergo $\mathbf{E} \times \mathbf{B}$ drift away from the spot along a trajectory in front of the plasma. (The electric field here is the space charge field of the expanding plasma and is directed normally out of the front surface.) In the simulations, a measure of this lateral transport process is proved by a plot of the net electron kinetic energy escape rate through the rear boundary of the computational mesh. In these simulations when an electron exits the plasma through this boundary, it is reintroduced back into the computational mesh at a point near its exit point but with a velocity obtained by sampling the initially assumed electron thermal spectrum. Thus a positive escape rate is a signature of superthermal electron escape. Figure 10 shows the rear-surface electron energy escape rate versus r for the cylindrical simulation, averaged over a time interval $22.5 \leqslant t \leqslant 27.0$ ps. The

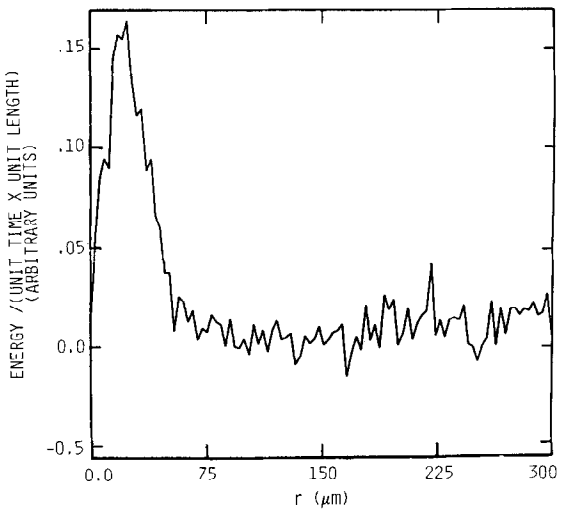

FIG. 10. Electron energy escape rate across the rear boundary ($z = 0$) of the mesh versus r for the cylindrical VENUS computation. The rate is averaged over the time interval $22.5 \leqslant t \leqslant 27.0$ ps.

large peak near $r = 0$ describes the loss of energetic electrons passing directly through the plasma from the spot region. (The escape rate vanishes at $r = 0$ because the cylindrical area factor $2\pi r$ vanishes.)

The small escape rate at intermediate r-values indicates that here electrons are unable to penetrate the **B** field and escape from the system. Finally at large r near the radial boundary of the plasma, there is a second significant contribution indicating some superthermal transport out to this point, where B_θ becomes vanishingly small. Considering energy loss out both the rear and radial boundaries, 17% of the source energy is transported by the superthermal electrons to radial distances greater than $\sim 110\,\mu$m from the edge of the laser spot and lost from the system in this time frame. This is a lower bound for the lateral transport of energy away from the spot. Comparison of this computation with the corresponding electrostatic simulation where $\mathbf{B} \equiv \mathbf{A} \equiv 0$ shows that the ions acquire 27% more energy in the full electrodynamic case during the time interval. This additional energy is that which is imparted to ions outside the spot by superthermal electrons laterally transported by the **B** field. As a result an additional 6% of the source energy is carried outside the spot region by superthermal electrons and deposited into ion energy, giving a total magnetic-field-induced lateral transport outside the spot of 23% of the source energy in the time frame. The general conclusion from this simulation is that significant superthermal lateral transport should be expected for the assumed experimental parameters on a time scale of tens of ps. One would arrive at a similar conclusion from the corresponding Cartesian simulation. Figure 11 shows the rear-surface energy escape plot for that simulation. Here, as in

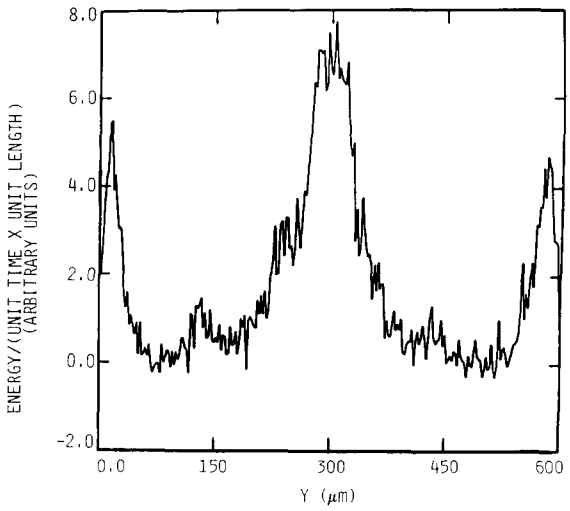

FIG. 11. Electron energy escape rate across the rear boundary ($x = 0$) of the mesh versus y for the Cartesian VENUS computation. The rate is averaged over the time interval $22.5 \leqslant t \leqslant 27.0$ ps.

the cylindrical case, there is a large contribution below the spot due to direct target penetration. And, as before, there is significant loss at large lateral distances from the spot, in this case near the y boundaries of the plasma where superthermal electrons propagate around the sides toward the rear boundary of the mesh. This simulation also indicates significant lateral transport away from the spot for the assumed experimental parameters on a time scale of tens of ps. In this case 20% of the source energy in the time frame appears as electron kinetic energy at distances greater than ~ 200 μm from the spot edge. This energy is, however, generally transported somewhat further from the laser spot than in the cylindrical case. Comparison with the corresponding electrostatic simulation shows that an additional 12% of the source energy is transported outside the spot and imparted to ions, a larger fraction than for the cylindrical case, giving a total of 32% of the source energy transported outside of the spot by the influence of the **B** field during the time interval under consideration. The differences in the results of the two simulations may be readily understood.

The distance the electrons are transported away from the spot before being drawn back into the plasma by the space charge **E** field depends on the spatial variation of the **B** field. In the Cartesian case, with B_z approximately constant in y away from the laser spot, a strong $\mathbf{E} \times \mathbf{B}$ drift, with small Larmor radius, across much of the front plasma surface can occur, producing considerable lateral transport. In the cylindrical case, with the rapid radial fall off of B_θ, the Larmor radius of the superthermal electrons becomes very large beyond a relatively short radial distance from the spot. Consequently these electrons will reenter the denser region

of the plasma, lateral transport ceases, and energy deposition to ions ceases. As a result there is less lateral transport than in the Cartesian case.

The two simulations show significant qualitative differences in both the self-generated magnetic fields and the lateral transport of superthermal electrons away from the laser spot. The underlying physical processes being simulated are the same, but the computed observables are different. These differences are readily understood, arising from differences in the geometry of the two simulations. But they point up the utility of employing a cylindrical mesh in the simulation of cylindrically symmetric experiments. The interpretation of computed results and the comparison of such results to experiment is then more direct.

5. Summary

The VENUS code, a two-dimensional electromagnetic PIC plasma simulator employing the implicit moment method, has been generalized so that computations may be performed in either a cylindrical or a Cartesian mesh. The implicit moment method makes possible the simulation of a complete experimental plasma over a much longer time duration than was previously possible with explicit techniques. In the implicit moment method, as in explicit PIC techniques, the system is advanced one time step by performing a particle advance and a field advance in succession. These two procedures must be modified in a consistent manner when a different coordinate system is to be employed. From a structural standpoint, the cylindrical particle mover does not differ greatly from the two-dimensional Cartesian particle mover, although there are some additional complications. Such a code may be readily developed from an existing Cartesian code with a few modifications, as shown in Section 2. Likewise the solution of the field equations in cylindrical coordinates closely follows the Cartesian method of solution in the implicit moment method. The significant modification is the addition of $1/r$- and $1/r^2$-terms to the

[redacted]

approximately cylindrically symmetrical experiments, making possible a more direct comparison of computational results and experimental data.

APPENDIX: Spatial Differencing

All field quantities are evaluated at cell centers $\mathbf{x}_g = (r_i, z_j)$, where

$$r_i = (i - \tfrac{1}{2})\,\Delta r, \qquad i = 1, 2, \ldots, i_{\max}, \tag{A.1}$$

$$z_j = (j - \tfrac{1}{2})\,\Delta z, \qquad j = 1, 2, \ldots, j_{\max}, \tag{A.2}$$

and

$$g = i + i_{\max}(j-1). \tag{A.3}$$

We denote a field at $\mathbf{x}_g$ by χ_{ij}. The first spatial derivatives are evaluated using the formulae

$$\left(\frac{\partial \chi}{\partial r}\right)_{i,j} = \frac{\chi_{i+1,j} - \chi_{i-1,j}}{2\Delta r}, \tag{A.4}$$

and

$$\left(\frac{\partial \chi}{\partial z}\right)_{i,j} = \frac{\chi_{i,j+1} - \chi_{i,j-1}}{2\Delta z}. \tag{A.5}$$

In our model where all quantities are independent of θ, all derivatives with respect to θ vanish. The resulting simplified expression for the gradient of a scalar χ is

$$(\nabla \chi)_{i,j} = \hat{r}\left(\frac{\partial \chi}{\partial r}\right)_{i,j} + \hat{k}\left(\frac{\partial \chi}{\partial z}\right)_{i,j}. \tag{A.6}$$

And the expression for the curl of a vector ξ is

$$(\nabla \times \xi)_{i,j} = -\hat{r}\left(\frac{\partial \xi_\theta}{\partial z}\right)_{i,j} + \hat{\theta}\left(\frac{\partial \xi_r}{\partial z} - \frac{\partial \xi_z}{\partial r}\right)_{i,j} + \hat{k}\left[\left(\frac{\partial \xi_\theta}{\partial r}\right)_{i,j} + \frac{(\xi_\theta)_{i,j}}{r_i}\right]. \tag{A.7}$$

The divergence of a vector ξ is evaluated using the formula

$$(\nabla \cdot \xi)_{i,j} = \frac{(\xi_r)_{i+1,j} r_{i+1} - (\xi_r)_{i-1,j} r_{i-1}}{2 r_i \Delta r} + \left(\frac{\partial \xi_z}{\partial z}\right)_{i,j}. \tag{A.8}$$

Putting the divergence in this form insures precise charge conservation with Eq. (1.25). The ∇^2-operator acting on a scalar is evaluated from

$$(\nabla^2 \chi)_{i,j} = \frac{\chi_{i+1,j} - 2\chi_{i,j} + \chi_{i-1,j}}{(\Delta r)^2} + \frac{\chi_{i+1,j} - \chi_{i-1,j}}{2 r_i \Delta r} + \frac{\chi_{i,j+1} - 2\chi_{i,j} + \chi_{i,j-1}}{(\Delta z)^2}. \tag{A.9}$$

And the ∇^2-operator acting on a vector is

$$(\nabla^2 \xi)_{i,j} = \hat{r}\left[(\nabla^2 \xi_r)_{i,j} - \frac{(\xi_r)_{i,j}}{r_i^2}\right] + \hat{\theta}\left[(\nabla^2 \xi_\theta)_{i,j} - \frac{(\xi_\theta)_{i,j}}{r_i^2}\right] + \hat{k}(\nabla^2 \xi_z)_{i,j}. \tag{A.10}$$

Finally, expressions of the form $\nabla \cdot \kappa \nabla \chi$, where κ is a scalar, are evaluated from

$$(\nabla \cdot \kappa \nabla \chi)_{i,j} = \left[\left(\frac{\kappa_{i+1,j}+\kappa_{i,j}}{2}\right)(\chi_{i+1,j}-\chi_{i,j}) - \left(\frac{\kappa_{i,j}+\kappa_{i,j-1}}{2}\right)(\chi_{i,j}-\chi_{i-1,j})\right]\frac{1}{(\Delta r)^2}$$
$$+\left[\left(\frac{\kappa_{i+1,j}+\kappa_{i,j}}{2}\right)(\chi_{i+1,j}-\chi_{i,j}) + \left(\frac{\kappa_{i,j}+\kappa_{i,j-1}}{2}\right)(\chi_{i,j}-\chi_{i-1,j})\right]\frac{1}{2r_i \Delta r}$$
$$+\left[\left(\frac{\kappa_{i,j+1}+\kappa_{i,j}}{2}\right)(\chi_{i,j+1}-\chi_{i,j}) - \left(\frac{\kappa_{i,j}+\kappa_{i,j-1}}{2}\right)(\chi_{i,j}-\chi_{i,j-1})\right]\frac{1}{(\Delta z)^2}. \quad \text{(A.11)}$$

The above formulae are used whenever spatial derivatives occur in the field equations.

ACKNOWLEDGMENT

The authors gratefully acknowledge useful discussions with A. B. Langdon.

REFERENCES

1. J. U. BRACKBILL AND D. W. FORSLUND, *J. Comput. Phys.* **46** (1982), 271.
2. R. J. MASON, *J. Comput. Phys.* **41** (1981), 233; *Phys. Rev. Lett.* **47** (1981), 652.
3. A. B. LANGDON AND D. C. BARNES, *in* "Computational Techniques: Multiple Time Scales" (J. U. Brackbill and B. I. Cohen, Eds.), Academic Press, Orlando, Fla., 1985.
4. J. U. BRACKBILL AND D. W. FORSLUND, *in* "Computational Techniques: Multiple Time Scales," (J. U. Brackbill and B. I. Cohen, Eds.), Academic Press, Orlando, Fla., 1985.
5. J. B. BORIS, Relativistic plasma simulation-optimization of a hybrid code, *in* "Proceedings of the Fourth Conference on Numerical Simulation of Plasmas," November 1970.
6. P. CONCUS AND G. H. GOLUB, *SIAM J. Numer. Anal.* **10** (1973), 1103.
7. C. W. NIELSON AND H. R. LEWIS, *Methods Comput. Phys.* **16** (1976), 367.
8. D. W. FORSLUND AND J. U. BRACKBILL, *Phys. Rev. Lett.* **48** (1982), 1614.